

Data-efficient iterative training of Gaussian approximation potentials: Application to surface structure determination of rutile IrO_2 and RuO_2

Cite as: J. Chem. Phys. **155**, 244107 (2021); <https://doi.org/10.1063/5.0071249>

Submitted: 13 September 2021 • Accepted: 08 November 2021 • Accepted Manuscript Online: 10 November 2021 • Published Online: 28 December 2021

 Jakob Timmermann,  Yonghyuk Lee, Carsten G. Staacke, et al.



View Online



Export Citation



CrossMark

ARTICLES YOU MAY BE INTERESTED IN

[Cumulants as the variables of density cumulant theory: A path to Hermitian triples](#)

The Journal of Chemical Physics **155**, 244105 (2021); <https://doi.org/10.1063/5.0076888>

[A tight-binding study of the electron transport through single-walled carbon nanotube-graphene hybrid nanostructures](#)

The Journal of Chemical Physics **155**, 244104 (2021); <https://doi.org/10.1063/5.0077099>

[Ising density functional theory for weak polyelectrolytes with strong coupling of ionization and intrachain correlations](#)

The Journal of Chemical Physics **155**, 241102 (2021); <https://doi.org/10.1063/5.0066774>

The Journal
of Chemical Physics

SPECIAL TOPIC: Low-Dimensional
Materials for Quantum Information Science

Submit Today!



Data-efficient iterative training of Gaussian approximation potentials: Application to surface structure determination of rutile IrO_2 and RuO_2

Cite as: J. Chem. Phys. 155, 244107 (2021); doi: 10.1063/5.0071249

Submitted: 13 September 2021 • Accepted: 8 November 2021 •

Published Online: 28 December 2021








View Online



Export Citation



CrossMark

Jakob Timmermann,  Yonghyuk Lee,  Carsten G. Staacke, Johannes T. Margraf,  Christoph Scheurer, 
and Karsten Reuter^{a)} 

AFFILIATIONS

Fritz-Haber-Institut der Max-Planck-Gesellschaft, Faradayweg 4-6, D-14195 Berlin, Germany

^{a)} Author to whom correspondence should be addressed: reuter@fhi-berlin.mpg.de

ABSTRACT

Machine-learning interatomic potentials, such as Gaussian Approximation Potentials (GAPs), constitute a powerful class of surrogate models to computationally involved first-principles calculations. At a similar predictive quality but significantly reduced cost, they could leverage otherwise barely tractable extensive sampling as in global surface structure determination (SSD). This efficiency is jeopardized though, if an *a priori* unknown structural and chemical search space as in SSD requires an excessive number of first-principles data for the GAP training. To this end, we present a general and data-efficient iterative training protocol that blends the creation of new training data with the actual surface exploration process. Demonstrating this protocol with the SSD of low-index facets of rutile IrO_2 and RuO_2 , the involved simulated annealing on the basis of the refining GAP identifies a number of unknown terminations even in the restricted sub-space of (1×1) surface unit cells. Particularly in an O-poor environment, some of these, then metal-rich terminations, are thermodynamically most stable and are reminiscent of complexions as discussed for complex ceramic materials.

Published under an exclusive license by AIP Publishing. <https://doi.org/10.1063/5.0071249>

I. INTRODUCTION

Machine-learning (ML) interatomic potentials trained with first-principles data promise steep advances for the predictive-quality modeling and simulation of molecules and materials.^{1–10} At a computational cost that is significantly reduced compared to direct first-principles calculations, such ML potentials allow us to address larger system sizes or perform more extensive dynamical simulations and sampling. While typically not as cost efficient as classical force fields with a fixed functional form, they straightforwardly allow us to include reactivity and, most importantly, can seamlessly be improved by additional training data.¹¹

This versatility also has its downsides though. With the ML potential itself completely void of any physics, the training data need to adequately cover the structural and chemical space of interest. Depending on the application, the underlying multiple first-principles calculations for the training data could then themselves start to become a computational bottleneck. The latter is, e.g., particularly pronounced for surface science or interfacial applications such

as heterogeneous catalysis or batteries. Therefore, training structures may necessarily extend to large supercell calculations, which even on an efficient semi-local density functional theory (DFT) level may constitute a formidable computational burden. This calls for data-efficient training protocols that achieve a reliable ML potential with a minimum number of DFT training data (of tractable system sizes).

A further complication in this respect is that the targeted chemical space may actually not be known *a priori* at the beginning of a study. Take the example of surface structure determination (SSD) that we want to specifically pursue here. We would like to use an ML potential to afford global structure determination techniques and identify unknown, possibly complex surface structures with non-bulk-like coordinations and chemical composition. If we do not know these structures beforehand, how can we make sure our training set covers all relevant local geometric and compositional motifs, while simultaneously being of minimum size?

The obvious solution to this challenge is to resort to iterative training protocols.¹² While exploring new parts of chemical

space, some form of uncertainty quantification will allow the ML potential to realize that it requires new pertinent training data. Corresponding new first-principles calculations will (ideally automatically) be initiated and the potential will be retrained. By now, a number of such iterative learning strategies have been reported, e.g., for elementary carbon or silicon,^{13–16} binary bulk materials such as zirconia,¹⁷ nanoparticles,^{12,18,19} and even for selected surface morphologies.²⁰ While conceptionally all similar, technical differences between these approaches extend from the ML model used (e.g., full or sparse kernel regression and neural networks) over the way the uncertainty is measured (e.g., committee/ensemble methods, Bayesian uncertainty, or dissimilarity to existing training data) to the way the automatized protocol is tailored to the targeted application [e.g., learning of the full potential energy surface (PES) or only of parts of it, with same or variable accuracy]. In this context, we here present and detail a two-stage highly data-efficient training protocol specifically geared toward surface structure determination and based on sparse Gaussian process regression (GPR). It consists of an initial bootstrapping, in which the existing domain knowledge on the system of interest is used to generate a suitable preliminary training set and arrive at a rudimentary ML potential that satisfactorily describes key physical properties. In a second stage, this training set is iteratively augmented and the potential is refined. Importantly, this refinement stage uses simulated annealing (SA) on the ML potential energy surface to efficiently sample the complex phase space of surface structures and identify new training structures as those that exceed a critical dissimilarity to those already computed at the first-principles level before. In this way, the training gets intimately intermingled with the actual global optimization process, and the evolving, minimum-size training set is ideally tailored to identify candidate structures that can subsequently be compared within an *ab initio* thermodynamics surface phase diagram.^{21,22}

We specifically demonstrate this approach by developing Gaussian Approximation Potentials (GAPs)^{1,23} for the surface structure determination of low-index rutile IrO₂ and RuO₂ facets. Both oxides are known as active oxidation catalysts in thermal catalysis and electrocatalysis, but equally known for their propensity to undergo surface structural and compositional changes under operating conditions.^{24–34} In preceding work by some of us,¹⁰ a GAP based surface structure determination could already identify hitherto unknown, so-called surface complexions for some IrO₂ facets. The iterative training of the potential was largely manual though and involved the addition of training structures based on visual inspection or the random addition of nanoparticle and high-temperature structures for a perceived training set diversity. Unsatisfied with this, we here revisit the problem with our automated training protocol that after the initial bootstrapping does not require any further human decision making. In turn, the bootstrapping set itself consists of those reference structures (bulk, molecular, and canonical surface terminations) that would always have been explicitly computed by first-principles in a surface structure determination project anyway. Gratifyingly, this new protocol identifies exactly the same complexions as the laboriously developed GAP potential before. Moreover, the transferability of the protocol is demonstrated by the application to RuO₂. In our preceding work, we had simply recomputed the identified IrO₂ complexions for this iso-structural oxide to demonstrate their stability. Intriguingly, the new protocol not only confirms

this but also reveals that RuO₂ surfaces, in fact, exhibit an even wider variety of these novel surface terminations.

II. METHODS

A. Gaussian approximation potentials

GAPs are a widely used class of interatomic ML potentials, based on Gaussian process regression. A detailed description is provided in the literature.^{1,23,35} For self-containment, we, therefore, provide here only a brief introduction to the formalism, emphasizing the aspects most relevant to this project.

1. Interatomic potential

The GAPs used herein are based on the combination of two-body (2B) and many-body (MB) contributions. This means that we calculate the total energy E_{GAP} of a system from its atomic coordinates \mathbf{X}_n as

$$E_{\text{GAP}}(\mathbf{X}_n) = \underbrace{\sum_{i,j} \delta_{2\text{B}}^2 \sum_{m=1}^{M_{2\text{B}}} c_{m,2\text{B}} k_{2\text{B}}(r_{ij}, r_m)}_{E_{2\text{B}}} + \underbrace{\sum_i \delta_{\text{MB}}^2 \sum_{m=1}^{M_{\text{MB}}} c_{m,\text{MB}} k_{\text{MB}}(\chi_i, \chi_m)}_{E_{\text{MB}}}. \quad (1)$$

Here, the first sum in $E_{2\text{B}}$ goes over all pairs of atoms i, j , and the first sum in E_{MB} goes over each atom i . The second sum in each term goes over a set of $M_{2\text{B}/\text{MB}}$ representative data points (the sparse set, see below) and contains the regression coefficients $c_{m,2\text{B}/\text{MB}}$ and the respective kernel functions $k_{2\text{B}/\text{MB}}$. The latter are used to measure the similarity between two geometric descriptors (representations), which are computed from \mathbf{X}_n . In the 2B case, these are simply interatomic distances r_{ij} . In the MB case, these are vectorial representations of the atomic environment χ_i , based on the Smooth Overlap of Atomic Positions (SOAP).^{1,23} A more detailed description of the kernel functions and representations used herein is given below. The final yet undefined parameters in Eq. (1) are $\delta_{2\text{B}}$ and δ_{MB} , which are used to specify the expected relative weighting of the two energy contributions.

While a full MB description of the interatomic potential is, in principle, possible, the explicit inclusion of a 2B term has been found to lead to significantly more stable and data-efficient potentials.¹³ The reason is that, due to its high flexibility, the high-dimensional representation used for the MB contribution extrapolates much more poorly than a simple 2B potential. The weighting specified by the δ parameters can, therefore, be used to switch between a less flexible but more robust potential with a strong 2B character and a highly flexible MB potential.

Assuming a given choice of kernel and representation (and a training database), this leaves the determination of the regression coefficients $c_{m,2\text{B}}$ and $c_{m,\text{MB}}$. In GAPs, these are obtained by minimizing the regularized least-squares loss function,

$$\ell = \sum_{n=1}^N \frac{|y_n - \bar{y}(\mathbf{X}_n)|^2}{\sigma_n^2} + R. \quad (2)$$

Here, R is a Tikhonov regularization term (see Ref. 35 for details), y_n are reference data points (in the present case, total energies and force components on all atoms of the training structures), and σ_n is an inverse weighting factor for a given data point. $\bar{y}(\mathbf{X}_n)$ indicates the GAP prediction for the property y_n , given the atomic coordinates \mathbf{X}_n based on the coefficients $c_{m,2B}$ and $c_{m,MB}$. Specifically, this means that energies are predicted according to Eq. (1) and force components by taking the corresponding derivative.

The role of the regularization term R is to penalize large regression coefficients, which indicate overfitting. As increasing the magnitude of σ_n increases the relative contribution of R to the loss function, these parameters are often called regularization strengths (particularly if a single parameter is used for all data points). Alternatively, they can be interpreted as the uncertainty associated with a given data point or the expected accuracy of the GAP. In other words, larger values of σ_n lead to a smoother potential, while smaller values lead to a more precise fit of the training set. Furthermore, using different values of σ_n for energies and forces allows adjusting the weight of these properties in the loss function.

2. Kernels and representations

The central components in the GAP energy expression of Eq. (1) are the kernel functions k_{2B} and k_{MB} and the corresponding geometric representations. Kernel functions are simply a similarity measure between representations usually ranging from 0 (not similar at all) to 1 (identical). In this sense, an intuitive explanation of a GAP model is that it predicts the energy of a configuration according to its similarity to other configurations in the training set. Since this similarity is defined by the choice of representations and kernels, these are critical to the performance of the model.

For the two-body contribution, the representation of a pair of atoms is simply its interatomic distance r_{ij} , and a squared exponential (Gaussian) kernel is used as a similarity measure,

$$k_{2B}(r_{ij}, r_m) = \exp\left(-\frac{\|r_{ij} - r_m\|^2}{2\sigma_{2B}^2}\right). \quad (3)$$

Inspecting Eq. (1), this means that E_{2B} is a pair potential, which consists of M_{2B} Gaussians of width σ_{2B} centered at the sparse points r_m (see below). Note that, in order to ensure size extensivity and favorable computational scaling, the two-body potential is constrained to be short-ranged. To this end, the cutoff parameter $r_{\text{cut},2B}$ is defined.

For the MB contribution to the potential, the SOAP representation and kernel are used. The main idea of SOAP is to generate a rotationally and permutationally invariant fingerprint of the local atomic environment within a sphere of radius $r_{\text{cut},\text{SOAP}}$ around a given central atom i . To this end, the environment is represented as a smooth density function ρ , which is obtained by smearing out the atomic positions of all atoms in the environment with Gaussian functions of width σ_{SOAP} . This density is then expanded with a set of basis functions centered on i , consisting of spherical harmonics and orthogonal radial functions. Finally, the corresponding expansion coefficients are transformed into the rotationally invariant power spectrum and collected in a normalized vector χ_i , which is the SOAP representation.

As a similarity measure, the SOAP representation is typically used with low-order polynomial kernels so that

$$k_{\text{MB}}(\chi_i, \chi_m) = (\chi_i \cdot \chi_m)^\zeta. \quad (4)$$

Herein, we use $\zeta = 2$ throughout. To fully define the SOAP representation, the number of radial and angular basis functions (n_{max} and l_{max}) needs to be specified.^{1,23}

3. Sparsification

An essential aspect of GAP models is that they use a sparse variant of Gaussian process regression (GPR). This is important because the training cost of full GPR models scales cubically with the number of training data points N (and the prediction cost linearly). This quickly becomes prohibitive for large training sets, in particular, when also training on forces (where each force component on each atom inside a training structure provides one data point). Sparse GPR models still use the full training set in the loss function, Eq. (2), but only use a sparse set of $M < N$ data points in the energy expression Eq. (1). In this manner, the training costs are substantially reduced and the energy prediction cost becomes formally independent of the training set size. Of course, this means that the sparse points need to be suitably selected.

For the two-body potential, this is achieved by placing the sparse points on a regular grid between zero and the cutoff length $r_{\text{cut},2B}$. For the high dimensional MB potential, such a grid would be extremely inefficient, however. If the training set is reasonably small (i.e., on the order of 1000 unique atomic environments per element), all atomic environments can be used as sparse points instead. For larger training sets, the most diverse environments of each species are selected using CUR decomposition.³⁶ Note that even if all environments are used, a GAP is always a sparse GPR model, as the full GPR model would use a regression coefficient for every single force component in the training set. This becomes prohibitive even for fairly small training sets so that training a GPR model on forces, in practice, always requires sparsification.

4. Kernel distance

In addition to being a crucial ingredient of the GAPs themselves, the SOAP kernel can also be used for selecting new training structures for the iterative training scheme described below. To obtain a data-efficient approach, it is important to ensure that the structures that are iteratively added to the training set are maximally different from training configurations already present in the set. As discussed above, SOAP measures the similarity of atomic environments and not of complete configurations of atoms, however. It is, therefore, common to use the averaged or matched similarities of the environments in two configurations for such a selection task.^{11,37} While this is very useful for comparing and mapping structures,³⁸ such global comparisons can overshadow the presence of a single unusual atomic environment, in an otherwise similar configuration. This is particularly prominent in surface applications, where inside the employed supercells, a dominant fraction of bulk-like atoms is always present in the inner layers of the slab. We, therefore, rather define the similarity of configurations A and B (where B could also be a group of different configurations) by the *minimal* similarity

$k_{\text{MB}}(\chi_a, \chi_b)$ between two atoms $a \in A$ and $b \in B$, where only identical species are compared. For convenience, we further convert this similarity provided by the SOAP kernel into a kernel distance using

$$\kappa(A, B) = \sqrt{2 - 2 \min_{\substack{a \in A \\ b \in B}} (k_{\text{MB}}(\chi_a, \chi_b))}, \quad (5)$$

where a larger distance $\kappa(A, B)$ indicates more dissimilar structures.

B. Density functional theory calculations

1. Computational settings

To achieve a predictive-quality GAP, all training data for both metallic oxides are computed with first-principles semi-local DFT using the revised Perdew–Burke–Erzerhof (RPBE)³⁹ functional to treat electronic exchange and correlation. The periodic boundary condition calculations are performed using a plane-wave basis set together with SG15 optimized norm-conserving Vanderbilt pseudopotentials⁴⁰ as implemented in the QuantumEspresso software package.⁴¹ The kinetic cutoff energy for the expansion of the wave function and the charge density are set to 80 and 320 Ry, respectively, and Brillouin zone integrations are performed with a uniform reciprocal distance of 0.02 \AA^{-1} . This generates $(11 \times 11 \times 16)$ k-point grids for both rutile IrO_2 and RuO_2 bulk unit cells and corresponding grids for the various surface supercell calculations. Optimized lattice parameters for both the oxides are obtained by minimizing the stress tensor and all internal degrees of freedom iteratively until the external pressure falls below 0.5 kbar. Geometry optimization for the surface calculations employed Broyden–Fletcher–Goldfarb–Shanno (BFGS) minimization^{42–44} until residual changes in total energy and all force components fell below $1.4 \times 10^{-2} \text{ meV}$ and 0.3 meV/\AA , respectively. At these computational settings, convergence tests detailed in the [supplementary material](#) demonstrate a high degree of convergence of the key quantities entering the GAP potential training, i.e., surface free energies to within 5 meV/atom and forces to within 50 meV/\AA .

2. Supercell setups

All five symmetry-inequivalent low-index surfaces (hkl) of rutile IrO_2 and RuO_2 are modeled via a supercell approach.^{24,33} Each slab model exposes a (1×1) surface unit cell and contains at least seven trilayers of MO_2 units (see Table S1 for a detailed list). A minimum vacuum region of 15 \AA thickness prevents interactions between periodic slabs. Truncation at different planes in the (hkl) crystal orientation generally gives rise to one metal-rich, one stoichiometric, and one oxygen-rich termination for all considered facets. One exception is (111), where two different stoichiometric terminations arise. Likewise, for the (001) facet, layered truncation leads only to a stoichiometric termination. Here, we, therefore, also consider one termination with an oxygen vacancy and one termination with an excess oxygen at the very top layer to build a metal-rich and oxygen-rich termination for this orientation, respectively. Under strongly oxidizing conditions, the rutile surfaces are, furthermore, known to stabilize peroxo-type surface moieties.^{24,33} One such peroxo-termination for each facet is also considered, with all structures further detailed in the [supplementary material](#).

3. Ab initio thermodynamics

In order to determine the relative stability of different surface structures in thermodynamic equilibrium with a surrounding oxygen-containing gas phase, we adopt the *ab initio* thermodynamics approach^{21,22} and calculate the surface free energy $\gamma_{\text{surf}}^{(hkl),\sigma}$ of a given crystallographic orientation (hkl) and termination σ as

$$\gamma_{\text{surf}}^{(hkl),\sigma} = \frac{1}{A^{(hkl)}} \left[G_{\text{surf}}^{(hkl),\sigma} - \sum_i n_i^{(hkl),\sigma} \mu_i \right]. \quad (6)$$

Here, $G_{\text{surf}}^{(hkl),\sigma}$ is the Gibbs free energy of the surface system with surface area $A^{(hkl)}$ and μ_i is the chemical potential of various species i [$i = \text{Ir}$ (or Ru) and O] present in the system. $n_i^{(hkl),\sigma}$ is the number of atoms of species i within the periodic supercell of the slab model.

Assuming the surface to be in thermodynamic equilibrium with the respective bulk MO_2 ($M = \text{Ir}$ or Ru) phase, we can connect the chemical potentials of metal (μ_M) and oxygen (μ_{O}) to the Gibbs free energy of MO_2 bulk, $G_{\text{MO}_2,\text{bulk}} = \mu_M + 2\mu_{\text{O}}$. The chemical potential of oxygen is instead set by the equilibrium with the surrounding gas phase. It is calculated as $\mu_{\text{O}} = \frac{1}{2}E_{\text{O}_2} + \Delta\mu_{\text{O}}$, with E_{O_2} being the total energy of an isolated O_2 molecule including zero point energy (ZPE) contributions⁴⁵ and the relative chemical potential $\Delta\mu_{\text{O}}$ allowing to connect to finite temperature and pressure (T, p).^{21,22} In the difference in Eq. (6), the condensed-phase Gibbs free energies are approximated by the DFT-computed total energies.²¹ The final working equation to determine the surface free energies, thus, reads

$$\gamma_{\text{surf}}^{(hkl),\sigma}(\Delta\mu_{\text{O}}) = \frac{1}{2A^{(hkl)}} \left[E_{\text{surf}}^{(hkl),\sigma} - n_m^{(hkl),\sigma} E_{\text{MO}_2,\text{bulk}} - \left(n_{\text{O}}^{(hkl),\sigma} - 2n_m^{(hkl),\sigma} \right) \left(\frac{1}{2}E_{\text{O}_2} + \Delta\mu_{\text{O}} \right) \right]. \quad (7)$$

C. Molecular dynamics simulations

1. Simulation details

All GAP based molecular dynamics (MD) simulations are performed with the LAMMPS code⁴⁶ and using the velocity Verlet algorithm as the time integrator.⁴⁷ The periodic boundary condition simulation cells contain (1×1) symmetric slabs with at least seven trilayers (see Table S1 for all unit-cell lattice vectors and slab thicknesses), separated by at least 15 \AA vacuum.

2. Simulated annealing

For the combined global geometry optimization and iterative identification of new structural motifs for GAP training, we employ a SA protocol. Exploiting the small volumetric thermal expansion coefficients for both IrO_2 and RuO_2 ,⁴⁸ the SA is carried out at a 1 fs time step within a canonical ensemble and only relies on an efficient Berendsen thermostat.⁴⁹ In the SA, the temperature is first raised from 200 to 1000 K for 500 ps. After that, the system is quenched back to 200 K within another 500 ps, i.e., we apply a constant heating and cooling rate of 1.6 K/ps. The initial GAP V_0 generated from the bootstrapping set (see below) still offers only a poor description of the potential energy surface, which is why for the SA in the very first refinement step we chose to only heat up to 500 K with a decreased heating and cooling rate of 0.8 K/ps.

The resulting finite temperature structure after each SA is finally fully optimized through conjugate gradient minimization with the same convergence threshold as used for the DFT calculations. For the surface structures contained in the initial training set, these optimized structures are obtained by minimization starting from the bulk-truncated geometries.

III. RESULTS AND DISCUSSION

A. Data-efficient simultaneous GAP training and surface exploration protocol

1. Bootstrapping

Our iterative GAP training protocol starts with a bootstrapping step, in which we assemble an initial dataset to establish a preliminary potential. This first GAP V_0 should fulfill certain minimum criteria regarding the anticipated chemistry of the targeted system and application. One guideline is, thus, to select training structures that optimally convey this chemistry and (largely) cure obvious teething problems such as non-physical atomic pair potentials or the (concomitant) instability of key reference structures. In view of data efficiency, another guideline is to select training structures that provide maximum information (e.g., in the form of symmetry-allowed forces on atoms) at a minimum DFT computational cost (e.g., for small supercell structures).

To the least, the GAP V_0 should cover the bulk reference states of the species in the system, i.e., here crystalline rutile MO_2 and the gas-phase O_2 dimer. Next to the mandatory atomic energies (in the case of oxygen provided as 1/2 of the O_2 energy), our initial training set, therefore, contains O_2 dimer data at varying O–O bond lengths that extend over the attractive, equilibrium, and repulsive parts of the DFT O–O binding energy curve. Analogously, it contains rutile MO_2 bulk unit cells at compressed, optimized, and decompressed DFT lattice parameters, as well as with displaced internal coordinates.

With a view on the intended surface structure determination, a final category of structures is spanned by different (1×1) terminations of all five rutile low-index facets, each time in a bulk-truncated geometry and in the DFT optimized geometry. Specifically, we include the 21 structures that result from systematically considering metal-rich, stoichiometric, and O-rich terminations, as well as terminations with an additional peroxo (–OO) group for all facets. The exact geometries of all structures in the, thus, resulting initial training set for both RuO_2 and IrO_2 are provided in an online repository.⁵⁰

2. Hyperparameter selection

As outlined in Sec. II, training a GAP requires selecting a series of hyperparameters. Most prominently, these are the δ -weights controlling the relative contributions of 2B and MB terms in Eq. (1) and the regularization parameters σ_n in Eq. (2). Herein, we use separate parameters σ_E and σ_F for energies and forces, respectively. Additionally, GAP requires the definition of the number of sparse points M_{2B} , M_{MB} . There are also a number of hyperparameters related to the choice of representations and kernels. In particular, both 2B potential and SOAP use a cutoff radius ($r_{\text{cut},2B}$, $r_{\text{cut},\text{SOAP}}$) for atomic interactions and both use a Gaussian broadening to control the smoothness of the representation (σ_{2B} , σ_{SOAP}). Finally, SOAP uses a

set of radial and angular basis functions to expand the atomic environment, the number of which is controlled by the parameters n_{max} and l_{max} .

The selection of these parameters is challenging in iterative training schemes. While it is possible to optimize the parameters on the bootstrapping set, it is unclear whether this choice is transferable to the larger training sets subsequently generated. Fortunately, reasonable heuristics and physical insight can be applied to mitigate this issue. For example, the weighting of 2B and MB contributions is estimated from the residual error of a pure two-body potential fit on the bootstrapping set. Here, it is important to note that these weights δ_{2B} , δ_{MB} are priors, which are multiplied with the regression coefficients in Eq. (1). This means that the actual contributions of the MB and 2B terms can deviate from these priors, if this allows minimizing the loss function (within the flexibility afforded by the regularization). Consequently, it is not necessary to redetermine the δ values every time the training set is increased. Similarly, the regularization parameters σ_E and σ_F are chosen to balance between overfitting and underfitting (see Fig. S6).

Meanwhile, the cutoff parameters $r_{\text{cut},2B}$ and $r_{\text{cut},\text{SOAP}}$ are related to the characteristic length scale of interatomic interactions in the material. These interactions result from a complex interplay of short-ranged chemical bonds, mid-ranged polarization and van der Waals effects, and long-ranged Coulomb interactions. It is, therefore, not *a priori* possible to decide on an appropriate cutoff length. Fortunately, the locality of interactions in a given material can be estimated by analyzing the induced forces on a reference atom when atoms at increasing distances are displaced in DFT calculations.¹³ A corresponding locality test for IrO_2 detailed in the [supplementary material](#) motivates using cutoffs of $r_{\text{cut},2B} = r_{\text{cut},\text{SOAP}} = r_{\text{cut}} = 5 \text{ \AA}$ in this study.

Given the cutoff, the remaining SOAP parameters (σ_{SOAP} , n_{max} , and l_{max}) determine how the atomic environment within the cutoff radius is described. As a general rule of thumb, we choose the number of radial functions (n_{max}) to be twice the number of angular functions (l_{max}), as it has been shown that using larger radial band limits than angular band limits generally leads to better accuracy for a given computational cost.³⁵ Herein, we find essentially converged performance on the bootstrapping set with $n_{\text{max}} = 8$ and $l_{\text{max}} = 4$ (see the [supplementary material](#)). The full set of hyperparameters used is compiled in Table I.

3. Assessment of initial GAP V_0

As intended, the initial GAP V_0 trained with the bootstrapping set displays stable reference structures. The optimum O_2 dimer distance exactly matches the DFT value of 1.22 \AA , and the optimum bulk MO_2 lattice parameters are within 0.5% of the corresponding DFT parameters. The O_2 binding energy and MO_2 bulk cohesive energies are reproduced within 16 and 25 meV/atom, respectively.

Gratifyingly, this local stability also extends already to most of the (1×1) low-index surface structures contained in the bootstrapping set. Figure 1 compiles the absolute differences of surface free energies $|\gamma_{\text{surf}}^{(hkl),\sigma}|$ computed with DFT and the preliminary GAP V_0 for these surfaces. Shown are the data not only for the (necessarily identical) bulk-truncated geometries but also after optimizing the structures on the respective potential energy surface (PES). This means that starting from the bulk-truncated surface geometry, the GAP structure is optimized on the GAP PES, while the

TABLE I. GAP hyperparameters employed in this work.

	r_{cut} (Å)	σ_{2B} (Å)	δ_{2B} (eV)	M_{2B}	σ_{SOAP} (Å)	n_{max}	l_{max}	δ_{MB} (eV)	M_{SOAP}	σ_{E} (eV)	σ_{F} (eV/Å)
IrO ₂	5.0	1.0	0.362	25	0.6	8	4	0.100	2000	0.001	0.01
RuO ₂	5.0	1.0	0.326	25	0.6	8	4	0.086	2000	0.001	0.01

DFT structure is optimized on the DFT PES, here and later always fully relaxing the entire slab.⁵¹ Figure 1 also compares the structural similarity of the two resulting minimum structures for each of the 16 IrO₂ surfaces as quantified by their kernel distance κ . With the notable exception of the (101) metal-rich termination, κ is smaller than 0.075 throughout, indicating a high similarity of the corresponding PES basins. We, thus, achieve already at this stage a highly satisfactory description of these PES parts of highest relevance for structure determination, as also evidenced by the consistently low error in the GAP surface free energies. Even the structurally and energetically much dissimilar GAP minimum structure for the (101) metal-rich termination does actually not reveal a major shortcoming of the initial GAP. Instead, it is, in fact, already a first success of the global structure determination to which we will return in more detail below.

Nevertheless and not surprisingly, the initial GAP is not perfect though. This is prominently reflected by a complete instability of the five peroxo terminated surfaces contained in the bootstrapping set. Upon GAP relaxation of the corresponding bulk-truncated geometries, the peroxo group always detaches to form an O₂ dimer. To analyze this problem and generally obtain insight into generated GAPs, we found an analysis of atom pair potentials (or atom binding energy curves) as shown in Fig. 2 to be a useful tool. This analysis is based on the number of local environments in the

current training set that actually conveys information of specific two-body distances between the atomic species. Contrasting this number as done in Fig. 2 with the predicted binding energy curves between two atomic species (here M–M, M–O, and O–O) readily discloses a possible lack of relevant information. Precisely, in distance ranges for which current training structures do not provide data, these binding curves tend to exhibit non-physical behavior, e.g., numerous minima or a lacking repulsive wall at short distances. Assessing the two-body distances contained in potential new training structures then shows whether they actually provide data on hitherto undersampled distance ranges. This provides a manual way to identify most meaningful new training structures, before the computationally demanding DFT calculations are actually initiated. In the present case, this type of analysis led us, for instance, to include the five peroxo terminations into the bootstrapping set in the first place, as they convey important information on shorter O–O distances. As apparent from Fig. 2, there is still a lack of relevant structural information at O–O distances around and above 1.5 Å, which is precisely the range relevant for the surface peroxo groups. The O–O pair potential correspondingly shows a non-physical form in this range, rationalizing why the peroxo groups decay into the more stable O₂ dimer within this initial GAP V_0 . In contrast, the relevant range of Ir–O and Ir–Ir distances is sampled quite well by the structures in the bootstrapping set. Correspondingly, the Ir–O

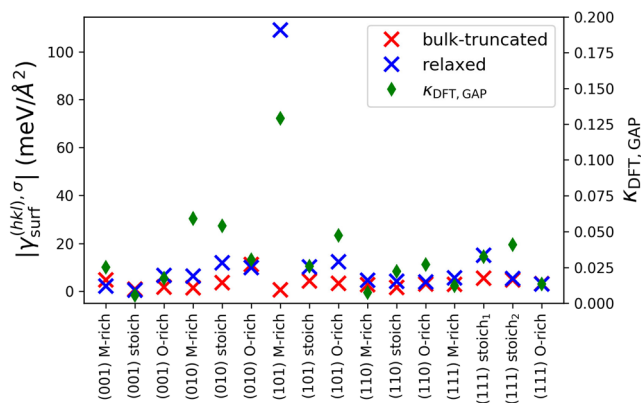


FIG. 1. Absolute difference of IrO₂ surface free energies $|\gamma_{\text{surf}}^{(hkl), \sigma}|$ computed by DFT and with the initial GAP V_0 for 16 different facets and (1×1) terminations contained in the bootstrapping training set. Shown are the data for the bulk-truncated geometries (red crosses) and optimized geometries (blue crosses). In the latter case, the optimization is performed on the corresponding potential energy surface, and the DFT and GAP structures compared are, thus, not necessarily the same. The shown kernel distance $\kappa_{\text{DFT, GAP}}$, cf. Eq. (5), provides a measure for this structural dissimilarity (green rhombuses). Analogous results for RuO₂ are shown in Fig. S8.

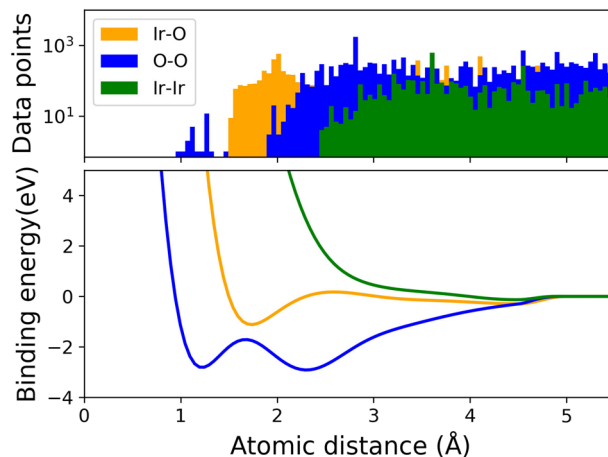


FIG. 2. Atom pair potential analysis for the initial GAP V_0 . (Bottom) GAP predicted binding energy as a function of distance between two Ir atoms, two O atoms, and an Ir–O atom pair. (Top) Number of local environments in the bootstrapping training set that provide corresponding two-body distances in their representation. Analogous results for RuO₂ are shown in Fig. S9.

and Ir–Ir pair potentials predicted by the GAP V_0 potential also look reasonable. The Ir–O potential shows one clearly defined minimum around distances corresponding to equilibrium distances in bulk IrO_2 . As the bootstrapping training set does not include Ir metal structures, the Ir–Ir pair potential instead is purely repulsive. This reflects the obvious fact that the training structures generally tailor the GAP for the intended application, and at least in its present form, this initial GAP V_0 would not be transferable to e.g., address oxide reduction to the parent metal.

4. Iterative refinement

While the atom pair potential analysis provides leads toward a manual addition of further training structures, we rather seek to establish a generic protocol that depends less on the chemical insight of the researcher. In a second stage of our training protocol, we, thus, refine the initial GAP V_0 in an iterative process. To ensure a high data efficiency, this process is specifically tailored for the intended use of surface structure determination. This use case requires a sufficiently precise representation of the PES basins that act as funnels into the distinct local minima, while the remaining PES only needs to be known to the extent that it shall not contain barriers between basins that are insurmountable by typical global optimization and PES exploration techniques. To some extent, we, thus, trade versatility for data efficiency and concentrate on exclusively identifying new meta-stable surface structures (PES minima) as additional training structures for the GAP. Obviously though, this concept is readily adapted to other use cases, notably, e.g., by selectively including transition states into the training when aiming for kinetics.

This specific basin-focused ansatz intrinsically blurs the lines between the iterative GAP training and the actual global geometry optimization, since the identified “novel” training structures are themselves already the sought-after, new, and dissimilar surface structures beyond the conventional terminations that were already included in the bootstrapping set. Here, we illustrate this concept by specifically exploring the chemical space of all low-index surface structures with (1×1) surface unit-cell periodicity. As detailed below, we reach a high data efficiency for this sub-space, identifying an intriguing, unknown class of surface structures termed complexions after having computed a minimum number of additional DFT structures. In future work, the final GAP trained this way could serve as a starting point for the exploration of larger surface unit-cell reconstructions, then iteratively adding corresponding structures to the training set. An additional challenge at this stage will arise when such structures extend over surface unit cells that are no longer tractable with direct DFT calculations, and thus, appropriate smaller models containing the same structural motifs need to be found for the training. One important aspect to this end could be the here pursued multi-task learning, i.e., training the GAP simultaneously for all five low-index facets. This creates a variety of structural motives already within the small (1×1) surface unit cells that otherwise would potentially have to be learned in larger surface unit cells when training the GAP only on a single facet.

For the present exploration of the chemical space of low-index (1×1) structures, we implement the iterative refinement process by executing the steps summarized in Fig. 3 at every refinement step s . Parallel SA runs based on the GAP V_{s-1} , which resulted from step

$s - 1$, are spawned for the 16 different surface types shown in Fig. 1. As the geometric details of the initial surface structure from which a SA is started are lost in the heating phase, we use these 16 different SAs primarily to sample the structural space of different chemical compositions and always start from the respective bulk-truncated terminations for simplicity. Note that our interest is here more in O-poor environments where the new complexions form (see below). This is why we do not further consider the highly O-rich peroxo terminations included in the bootstrapping set, but seek to obtain training data for short O–O distances otherwise.

After cooldown and optimization, we then arrive at 16 new GAP basin candidates $\text{BC}_{\text{GAP}}^{(hkl),\sigma}(s)$ in each refinement step s . Each candidate is compared to all previously identified basins $\{\text{B}^{(hkl),\sigma}\}$ of the same Miller index (hkl) and termination σ using the kernel distance κ , cf. Eq. (5). Figure 4 shows the evolution of κ during six selected SA runs in the first refinement step $s = 1$, where $\{\text{B}^{(hkl),\sigma}\}$ consists for each (hkl, σ) only of the corresponding bulk-truncated and DFT-optimized surface structure contained in the initial bootstrapping set. In two of the shown SA runs (as well as in the other ten not-shown ones), κ decreases back to essentially zero after cooldown and the subsequent geometry optimization, indicating that the candidate structure has collapsed back into the known basin from the bootstrapping set. In contrast, in four runs, finite values $\kappa > 0.075$ remain during cooldown and optimization. Visual inspection, cf. Fig. 4, reveals that in all four cases, a new PES basin with a distinct structure has been found. Based on this experience in the first refinement step, we employ $\kappa_{\text{crit}} = 0.075$ as a system-specific parameter for all later steps $s > 1$ and classify a GAP basin candidate as hitherto not known, if it exhibits a $\kappa > \kappa_{\text{crit}}$ with respect to all previously assembled basins $\{\text{B}^{(hkl),\sigma}\}$.

Every new GAP basin candidate is subsequently subjected to a DFT optimization to obtain DFT basin candidate $\text{BC}_{\text{DFT}}^{(hkl),\sigma}(s)$. If this does not lead to any significant structural changes with respect to $\text{BC}_{\text{GAP}}^{(hkl),\sigma}(s)$, here and henceforth indicated again by a similarity measure $\kappa < \kappa_{\text{crit}}$, then there is no need to consider both similar structures in the GAP training, and only the new DFT basin structure $\text{BC}_{\text{DFT}}^{(hkl),\sigma}(s)$ is added to the pool of known basins $\{\text{B}\}$. If there is a significant structural difference and the DFT basin structure was not known, then both the GAP basin candidate $\text{BC}_{\text{GAP}}^{(hkl),\sigma}(s)$ and the DFT basin candidate $\text{BC}_{\text{DFT}}^{(hkl),\sigma}(s)$ are added to the pool. If, instead, there is a significant structural difference between $\text{BC}_{\text{GAP}}^{(hkl),\sigma}(s)$ and $\text{BC}_{\text{DFT}}^{(hkl),\sigma}(s)$, but $\text{BC}_{\text{DFT}}^{(hkl),\sigma}(s)$ was already known, then the current GAP potential V_s provides apparently only an insufficient representation of this known basin. Since the DFT basin is already contained in the pool of known basins, only the new GAP basin candidate $\text{BC}_{\text{GAP}}^{(hkl),\sigma}(s)$ is added in this case.

As shown in Fig. 3, this iterative process is repeated until no further new basin candidate is added to the pool in refinement step s . At this point, we declare the training protocol as converged and conclude that all relevant energetically low-lying PES minima in the sampled sub-space of (1×1) surface unit cells have been found. Note that this situation arises only when no unknown basins are found, and the last GAP refinement $V_{s-1} \rightarrow V_s$ has not led to any significant structural relaxation of previously found GAP basins. In the present application to the rutile oxides, this convergence is quickly reached in $s = 12$ iterations. The final pool of known basins

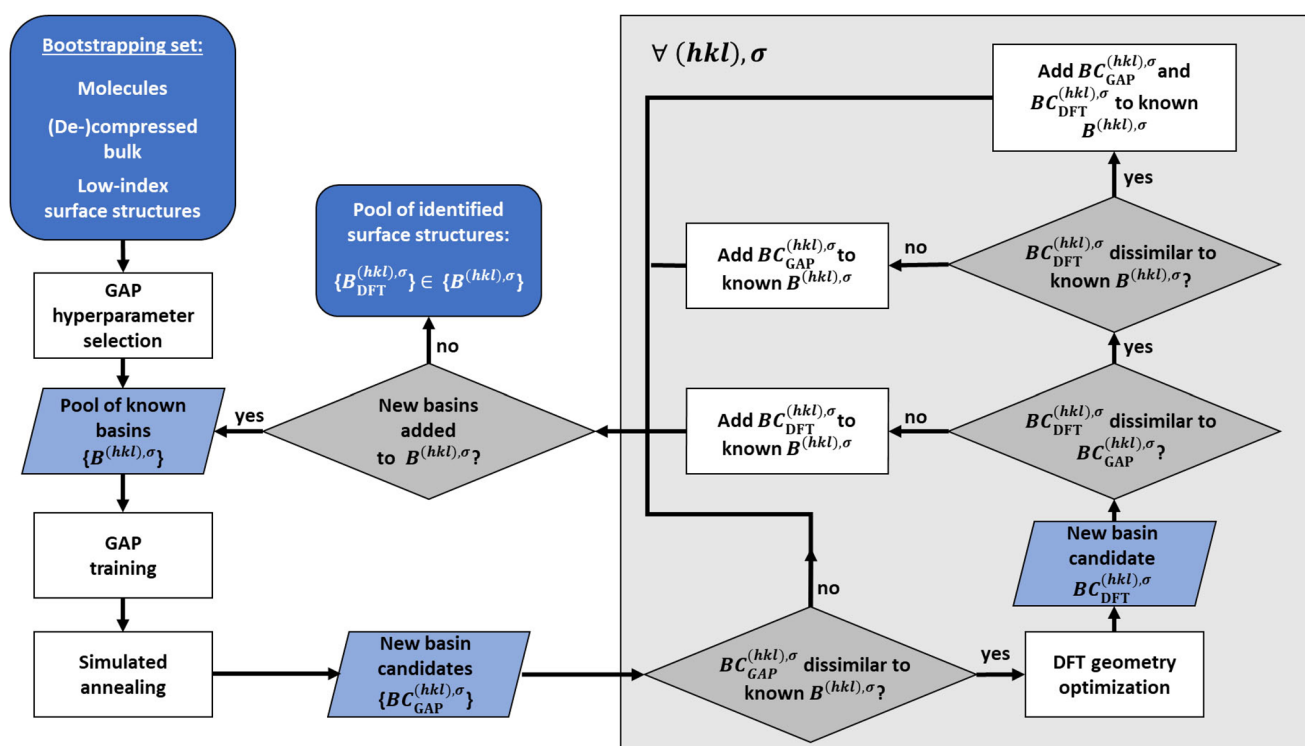


FIG. 3. Flowchart of the iterative GAP training protocol.

contains an additional 80 structures for IrO_2 and 63 structures for RuO_2 beyond the 32 surface structures already contained in the bootstrapping set. Of these, 53 (IrO_2) viz., 43 (RuO_2) correspond to DFT optimized geometries, with the remaining ones corresponding to GAP optimized geometries. All structures are provided in an online repository.⁵⁰

Adding a GAP optimized geometry to the training set requires only a DFT single-point calculation. Compared to this, the DFT geometry optimization of a (1×1) surface structure required to add a DFT optimized geometry to the training set is computationally much more demanding. In this respect, the fact that for the exploration of the sub-space of all low-index (1×1) surface structures, only 53 (IrO_2) viz., 43 (RuO_2) such optimizations are needed attests to the high data efficiency of our approach. While this does, in fact, not constitute any significant computational burden on modern supercomputing architectures, we, nevertheless, chose to further increase the computational efficiency of our approach by thresholding the costs for these DFT geometry optimizations. For this, any optimization is stopped, if relaxation is not achieved within the first 20 geometry steps. In this case, we simply employ the last geometry as a sufficient proxy for $BC_{DFT}^{(hkl),\sigma}(s)$ for the purpose of differentiating known and unknown basins. Further increases in efficiency could be reached by performing the SAs only for subsets of all surface orientations and terminations, e.g., selected on the basis of farthest point sampling of structural dissimilarity of all acquired basins at the time. Yet, all of this will only start to play a role when extending the global

geometry optimization to larger surface unit cells and will be the topic of future work in our group.

B. Novel structures and surface phase diagram

As mentioned above, the iterative refinement blends GAP training with the actual surface structure exploration, i.e., the basins accumulated in the final GAP training pool constitute at the same time the result of the SA-based global geometry optimization. It is worthwhile to emphasize the elegant efficiency of this approach: The extensive energy and force evaluations underlying the SA PES exploration are performed at the undemanding GAP level, while novel identified basins are immediately validated by computationally less demanding DFT geometry optimization as part of the training protocol. Every DFT basin contained in the final pool of GAP training structures is, therefore, already intrinsically validated at the first-principles level. Of course, not all of these meta-stable PES minima are physically really relevant. Many are likely energetically rather unfavorable and were only added to the training pool to pinpoint specific structural motives for the GAP.

Thermodynamically relevant is instead at best only the lowest-energy structure within each $(hkl), \sigma$ class, i.e., defined facet orientation and surface stoichiometry. In this respect, the resulting pool of structures is highly intriguing and underscores impressively the necessity of global geometry optimization for reliable surface structure determination. Even though the sub-space of structures

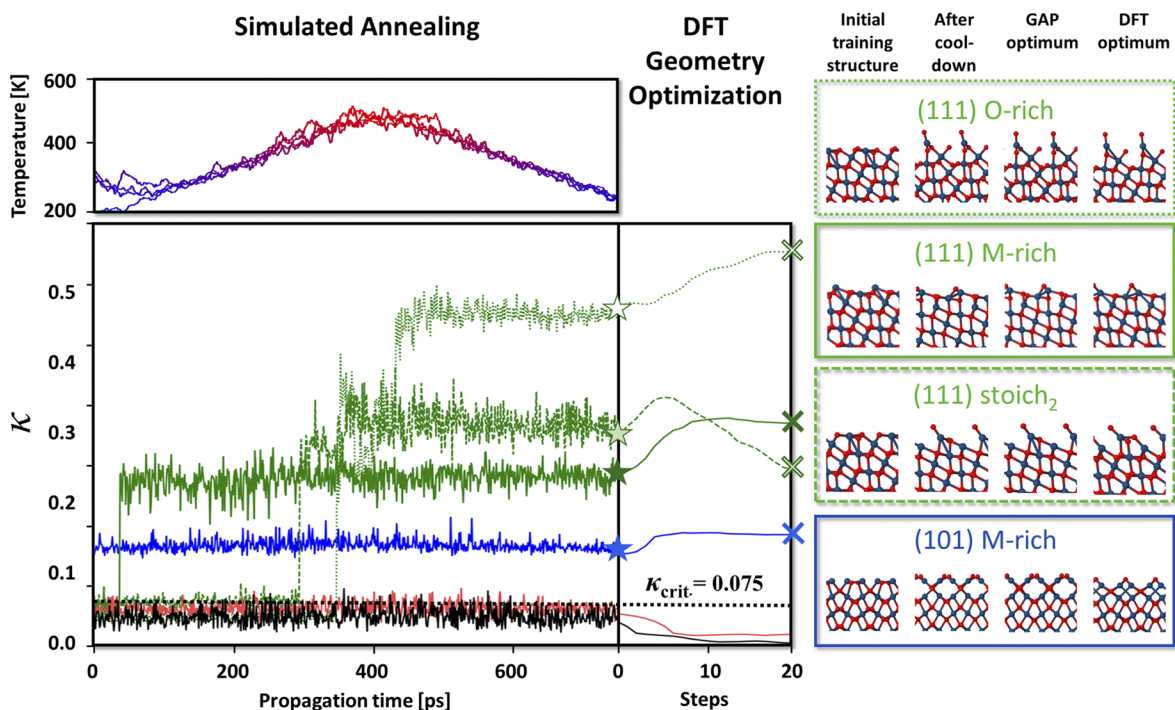


FIG. 4. (Left panel) Evolution of the kernel distance κ during six of the 16 SA runs of the first GAP refinement step $s = 1$ for IrO_2 . κ generally measures the similarity of the SA structure to all previously found basins $\{B^{(hkl),\sigma}\}$ of the same Miller index (hkl) and termination σ . In two cases [(010) O-rich, solid red line, (001) O-rich, solid black line], the SA does not lead to a new structure as reflected by the small κ value. In four cases, the SA identifies a new structure as reflected by $\kappa > \kappa_{crit} = 0.075$. (Right panel) Side views illustrating the identified new structures (Ir atoms drawn as larger blue spheres and O atoms as smaller red spheres). Shown for all four cases are the initial training structure, the structure obtained after cooldown, and the structures obtained after the final GAP and DFT geometry optimization (see main text). The κ values of these optimized geometries are additionally highlighted in the left panel as correspondingly colored stars (GAP PES minimum) and crosses (DFT PES minimum).

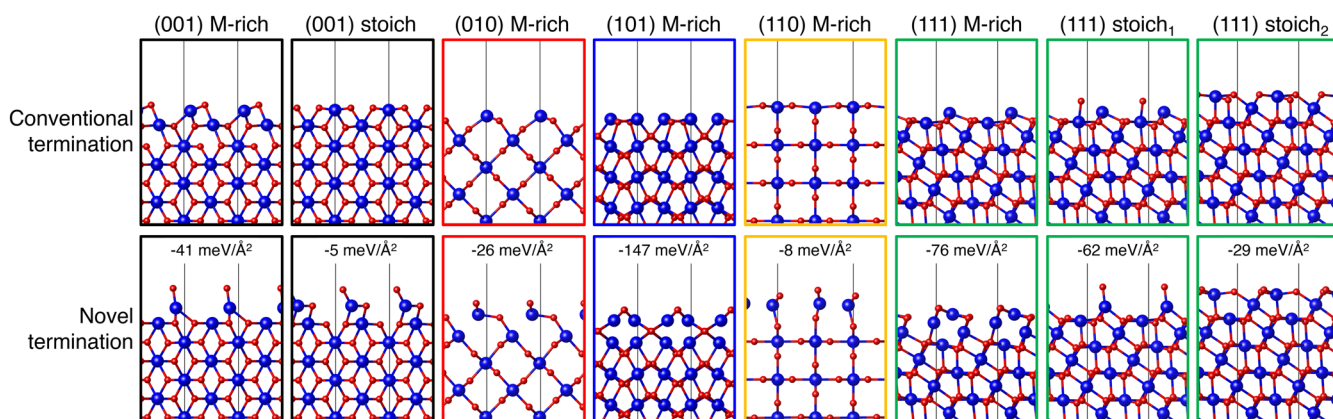


FIG. 5. Unconventional and energetically more stable (1×1) IrO_2 surface structures identified during the GAP training and surface exploration protocol. Top row: side view of the conventional $(hkl), \sigma$ termination resulting from truncating the bulk oxide-layering sequence and subsequent DFT geometry optimization. Bottom row: side view of the identified most stable structure, with the relative difference in surface free energy stated explicitly [see main text for the (101) metal-rich termination]. Ir atoms are drawn as larger blue spheres and O atoms are drawn as smaller red spheres. The color coding of the figure frames is consistent with that of the κ trajectories in Fig. 4. Analog results for RuO_2 are shown in Fig. S10.

with (1×1) surface unit cells was initially only chosen for the methodological development of the training and exploration protocol, energetically lower-lying terminations are, in fact, identified for eight (IrO_2) and seven (RuO_2) of the 16 $(hkl), \sigma$ classes. In other words, even within the restricted structural possibilities of these small unit cells, more stable alternatives to the conventionally considered simple truncations of the bulk oxide-layering sequence are for both oxides found in about half of the cases.

As detailed for IrO_2 in Fig. 5, these unconventional structures extend over metal-rich and stoichiometric surface compositions, and are in many cases energetically significantly more stable than their conventionally considered bulk-layered counterparts. Partly, the new structures are somewhat obvious and may, thus, potentially also have been tested as part of a human-devised set of trial candidate structures. This concerns notably open structures such as those of the (001) metal-rich or (111) stoichiometric class, where terminal O atoms do not occupy the (relaxed) sites corresponding to the next layer in the bulk-layering sequence, but instead to the second next one. However, especially for the (101) metal-rich and (111) metal-rich class, the novel structures with their concomitant strong energetic lowerings are quite counter-intuitive and had never been reported in the literature before our preceding work.¹⁰ Once understood, they are conceptually straightforward, too, though. They correspond to a reordering of the layering sequence, in which a terminal metal layer swaps its position with an oxygen layer and, thereby, achieves a higher O-coordination for its metal atoms.

For the (101) metal-rich termination, the concomitant stabilization is, in fact, so strong that the conventional termination is not even a local minimum on the DFT PES anymore. It relaxes barrierlessly into the reordered structure, which is why we state the relative energy lowering in Fig. 5 with respect to the artificial bulk-truncated and unrelaxed conventional termination. For IrO_2 , this conventional termination is spuriously (meta-)stabilized when only relaxing a finite number of outermost slab layers (and freezing innermost slab layers) as is typically done in DFT geometry optimization. As this was also done in the creation of the bootstrapping training set, this conventional (101) metal-rich termination is part of the IrO_2 set. As noted above, the entire slab is instead flexible in the GAP SA runs and subsequent DFT optimizations, and even the preliminary GAP V_0 then immediately led to this new structure, as reflected by the high kernel distance κ for this (101) metal-rich class in Fig. 1. In contrast, for RuO_2 , the conventional termination is never meta-stable, even if only a few outermost layers are relaxed during the DFT geometry optimization, cf. Fig. S8.

Whether or not the identified, novel lower-energy structures play a role thermodynamically depends on the environment to which the oxide is exposed. Here, we specifically consider an oxygen atmosphere. Figure 6 correspondingly shows the surface phase diagram for IrO_2 and RuO_2 in the explored sub-space of (1×1) surface structures as a function of the oxygen chemical potential of this surrounding gas phase. Within the *ab initio* thermodynamics approach,^{21,22} such a surface phase diagram is constructed by computing the surface free energy, $\gamma_{\text{surf}}^{(hkl), \sigma}(\Delta\mu_{\text{O}})$ of Eq. (7) for each DFT-optimized basin and plotting for each $\Delta\mu_{\text{O}}$ only the lowest energy one for each of the five facets. In the specific case of the here explored (1×1) structures, the lines in the resulting surface phase diagram are easily read. A positive slope indicates the

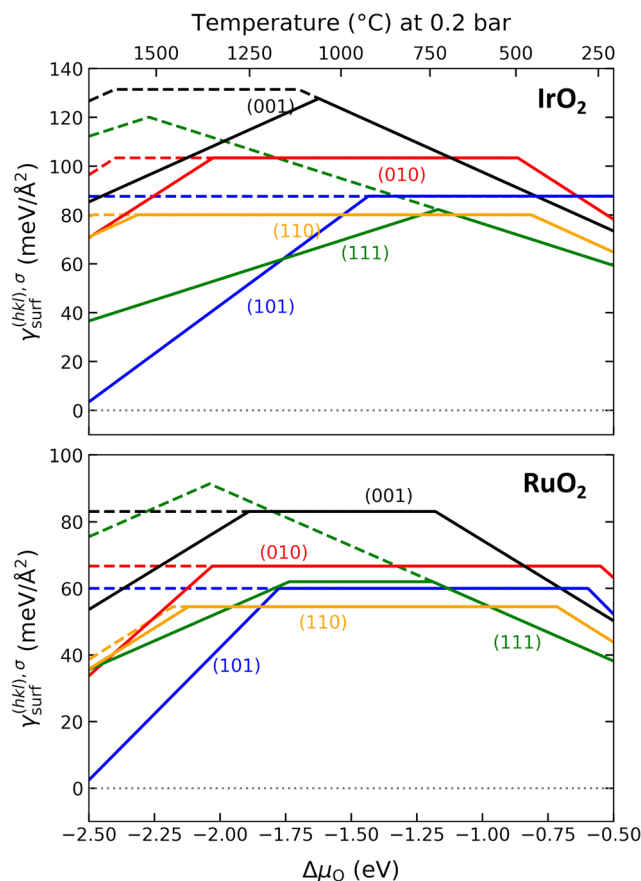


FIG. 6. DFT surface free energies $\gamma_{\text{surf}}^{(hkl), \sigma}$ of the five symmetry-inequivalent low-index facets of IrO_2 (top) and RuO_2 (bottom) in a pure oxygen atmosphere. In the top x axis, the dependence on the oxygen chemical potential $\Delta\mu_{\text{O}}$ is translated into a temperature scale at 0.2 bar pressure (the oxygen partial pressure in air). Shown is for each facet only the surface free energy of the most stable termination at each chemical potential. Each kink in the corresponding line indicates, therefore, the change to a different termination with a different stoichiometry. The dashed lines indicate the surface free energies when only considering the conventional (relaxed) bulk oxide-layered terminations (see main text).

stability of a metal-rich termination in the corresponding range of oxygen chemical potentials, a horizontal line indicates the stability of a stoichiometric termination, and a negative slope indicates the stability of an O-rich termination. Any kink in the continuous line representing one facet orientation, therefore, reflects a change to a more stable termination with a different stoichiometry.

As apparent from Fig. 6, quite some changes are induced by the novel structures as compared to the surface phase diagram when only considering the conventional bulk oxide-layered terminations.^{10,33} Notably, this extends to O-poor conditions, where the novel metal-rich (101) structure results as, by far, most stable for both oxides. For IrO_2 , this intriguing result (and first-principles prediction) has been validated by experimental work on crystals grown under corresponding O-poor conditions.¹⁰ Detailed surface science characterization confirmed the dominance of the (101) facet

and the specific geometry of this novel structure. Accompanying calculations showed that no further stability gains can be reached by a reordering of deeper layers. This places this novel structure close to so-called complexions as discussed for complex ceramic materials.⁵² These complexions possess a thermodynamically determined equilibrium thickness on the order of nanometers, but are thin versions of neither a known 3D bulk phase nor a reconstructed surface layer. In this preceding work, a recomputation of this complexed (101) metal-rich termination for RuO₂ suggested that this novel structure should also be stabilized for this oxide. As seen in Fig. 6, we can now confirm this on the basis of the proper surface exploration performed for this material. At the same time, it is also for RuO₂ that the literature already tells that the surface phase diagrams on the basis of the sub-space of (1 × 1) surface unit cells cannot yet be complete: The deactivation of this catalyst for CO oxidation had been assigned to the formation of a c(2 × 2) reconstruction of the (010) facet.³⁴ Extending the data-efficient GAP training and exploration protocol to such larger surface unit cells correspondingly forms the natural next topic of our work.

IV. CONCLUSIONS AND OUTLOOK

We have presented a protocol for surface structure determination through a surrogate ML potential that achieves high efficiency with regard to the required first-principles calculations by mixing the potential training and surface exploration. In an iterative process, the employed GAP identifies novel structures through extensive SA-based sampling of the potential energy surface and is refined by adding sufficiently dissimilar structures to its training pool. In its construction, this protocol is aimed for general usage. Here, we have illustrated it with the application to surface structure determination of low-index facets of rutile IrO₂ and RuO₂ within the sub-space of structures with (1 × 1) surface unit cells. Intriguingly, already in this restricted space, a number of non-intuitive low-energy structures are identified that would potentially have escaped the more traditional approach of testing a set of candidate structures devised by the researcher.

The obvious next step in developing an automatized workflow for surface structure determination in less restricted structural spaces would be to consider larger surface unit cells, e.g., to address some known surface reconstruction. For tractable unit-cell sizes, the present protocol should, in principle, be readily applicable. For one, one would only face concomitantly larger computational costs for each required DFT training structure. More problematic is the larger range of different possible surface stoichiometries, as the actual surface composition is generally not known, even if the surface unit cell is. For the here considered sub-space of (1 × 1) structures, this compositional range comprised metal-rich, stoichiometric, and oxygen-rich compositions. Many more relative compositions would have to be considered for general (*m* × *n*) surface unit cells in the present approach rooted on separate, canonical PES sampling. Ultimately, grand-canonical schemes could become appealing, but would have to be appropriately integrated into the GAP training. A final grand challenge arises in the context of completely unbiased surface structure determination extending over surface unit cells of unknown size and shape. To the least, schemes will need to be developed that extract those local environments and

geometric motives deemed important for the ML potential training into surface unit cells that can still be accessed by first-principles calculations.

SUPPLEMENTARY MATERIAL

See the [supplementary material](#) for the details of DFT convergence tests, bulk-truncated surface structures, hyperparameter selections for regularization parameters and the cutoff radius, and results for RuO₂.

ACKNOWLEDGMENTS

This research was supported by the Kopernikus/P2X programme of the German Federal Ministry of Education and Research, the German Federal Environmental Foundation DBU, and the German Academic Exchange Service DAAD.

AUTHOR DECLARATIONS

Conflict of Interest

The authors have no conflicts of interest to disclose.

DATA AVAILABILITY

The data that support the findings of this study are openly available at <https://doi.org/10.6084/m9.figshare.16610488>.⁵⁰

REFERENCES

- 1 A. P. Bartók, M. C. Payne, R. Kondor, and G. Csányi, *Phys. Rev. Lett.* **104**, 136403 (2010).
- 2 J. Behler, *J. Chem. Phys.* **134**, 074106 (2011).
- 3 M. Rupp, A. Tkatchenko, K.-R. Müller, and O. A. Von Lilienfeld, *Phys. Rev. Lett.* **108**, 058301 (2012).
- 4 J. C. Snyder, M. Rupp, K. Hansen, K.-R. Müller, and K. Burke, *Phys. Rev. Lett.* **108**, 253002 (2012).
- 5 K. Hansen, G. Montavon, F. Biegler, S. Fazli, M. Rupp, M. Scheffler, O. A. Von Lilienfeld, A. Tkatchenko, and K.-R. Müller, *J. Chem. Theory Comput.* **9**, 3404 (2013).
- 6 F. Brockherde, L. Vogt, L. Li, M. E. Tuckerman, K. Burke, and K.-R. Müller, *Nat. Commun.* **8**, 872 (2017).
- 7 O. A. Von Lilienfeld, *Angew. Chem., Int. Ed.* **57**, 4164 (2018).
- 8 J. Schmidt, C. L. Benavides-Riveros, and M. A. L. Marques, *J. Phys. Chem. Lett.* **10**, 6425 (2019).
- 9 M. Bogojeski, L. Vogt-Maranto, M. E. Tuckerman, K.-R. Müller, and K. Burke, *Nat. Commun.* **11**, 5223 (2020).
- 10 J. Timmermann, F. Kraushofer, N. Resch, P. Li, Y. Wang, Z. Mao, M. Riva, Y. Lee, C. Staacke, M. Schmid, C. Scheurer, G. S. Parkinson, U. Diebold, and K. Reuter, *Phys. Rev. Lett.* **125**, 206101 (2020).
- 11 S. Stocker, G. Csányi, K. Reuter, and J. T. Margraf, *Nat. Commun.* **11**, 5505 (2020).
- 12 R. Jinnouchi, K. Miwa, F. Karsai, G. Kresse, and R. Asahi, *J. Phys. Chem. Lett.* **11**, 6946 (2020).
- 13 V. L. Deringer and G. Csányi, *Phys. Rev. B* **95**, 094203 (2017).
- 14 A. P. Bartók, J. Kermode, N. Bernstein, and G. Csányi, *Phys. Rev. X* **8**, 041048 (2018).
- 15 D. Dragoni, T. D. Daff, G. Csányi, and N. Marzari, *Phys. Rev. Mater.* **2**, 013808 (2018).

- ¹⁶P. Rowe, V. L. Deringer, P. Gasparotto, G. Csányi, and A. Michaelides, *J. Chem. Phys.* **153**, 034702 (2020).
- ¹⁷C. Verdi, F. Karsai, P. Liu, R. Jinnouchi, and G. Kresse, *npj Comput. Mater.* **7**, 156 (2021).
- ¹⁸E. L. Kolsbjerg, A. A. Peterson, and B. Hammer, *Phys. Rev. B* **97**, 195424 (2018).
- ¹⁹S. Kaappa, E. G. del Río, and K. W. Jacobsen, *Phys. Rev. B* **103**, 174114 (2021).
- ²⁰M. K. Bisbo and B. Hammer, *Phys. Rev. Lett.* **124**, 086102 (2020).
- ²¹K. Reuter and M. Scheffler, *Phys. Rev. B* **65**, 035406 (2001).
- ²²K. Reuter, *Catal. Lett.* **146**, 541 (2016).
- ²³V. L. Deringer, M. A. Caro, and G. Csányi, *Adv. Mater.* **31**, 1902765 (2019).
- ²⁴D. Opalka, C. Scheurer, and K. Reuter, *ACS Catal.* **9**, 4944 (2019).
- ²⁵T. Reier, D. Teschner, T. Lunkenbein, A. Bergmann, S. Selve, R. Kraehnert, R. Schlögl, and P. Strasser, *J. Electrochem. Soc.* **161**, F876 (2014).
- ²⁶P. Steegstra, M. Busch, I. Panas, and E. Ahlberg, *J. Phys. Chem. C* **117**, 20975 (2013).
- ²⁷D. F. Abbott, D. Lebedev, K. Waltar, M. Povia, M. Nachtegaal, E. Fabbri, C. Copéret, and T. J. Schmidt, *Chem. Mater.* **28**, 6591 (2016).
- ²⁸S. Cherevko, S. Geiger, O. Kasian, A. Mingers, and K. J. J. Mayrhofer, *J. Electroanal. Chem.* **774**, 102 (2016).
- ²⁹E. Willinger, C. Massué, R. Schlögl, and M. G. Willinger, *J. Am. Chem. Soc.* **139**, 12093 (2017).
- ³⁰P. Lettenmeier, J. Majchel, L. Wang, V. A. Saveleva, S. Zafeiratos, E. R. Savinova, J.-J. Gallet, F. Bournel, A. S. Gago, and K. A. Friedrich, *Chem. Sci.* **9**, 3570 (2018).
- ³¹P. Lettenmeier, L. Wang, U. Golla-Schindler, P. Gazdzicki, N. A. Cañas, M. Handl, R. Hiesgen, S. S. Hosseiny, A. S. Gago, and K. A. Friedrich, *Angew. Chem., Int. Ed.* **128**, 752 (2016).
- ³²Q. Sun, K. Reuter, and M. Scheffler, *Phys. Rev. B* **67**, 205424 (2003).
- ³³T. Wang, J. Jelic, D. Rosenthal, and K. Reuter, *ChemCatChem* **5**, 3398 (2013).
- ³⁴J. Aßmann, D. Crihan, M. Knapp, E. Lundgren, E. Löffler, M. Muhler, V. Narkhede, H. Over, M. Schmid, A. P. Seitsonen, and P. Varga, *Angew. Chem., Int. Ed.* **44**, 917 (2005).
- ³⁵V. L. Deringer, A. P. Bartók, N. Bernstein, D. M. Wilkins, M. Ceriotti, and G. Csányi, *Chem. Rev.* **121**, 10073 (2021).
- ³⁶A. P. Bartók and G. Csányi, *Int. J. Quantum Chem.* **115**, 1051 (2015).
- ³⁷J. S. De Almeida and R. Ahuja, *Phys. Rev. B* **73**, 165102 (2006).
- ³⁸B. Cheng, R.-R. Griffiths, S. Wengert, C. Kunkel, T. Stenzel, B. Zhu, V. L. Deringer, N. Bernstein, J. T. Margraf, K. Reuter, and G. Csányi, *Acc. Chem. Res.* **53**, 1981 (2020).
- ³⁹B. Hammer, L. B. Hansen, and J. K. Nørskov, *Phys. Rev. B* **59**, 7413 (1999).
- ⁴⁰D. R. Hamann, *Phys. Rev. B* **88**, 085117 (2013).
- ⁴¹P. Giannozzi, S. Baroni, N. Bonini, M. Calandra, R. Car, C. Cavazzoni, D. Ceresoli, G. L. Chiarotti, M. Cococcioni, I. Dabo, A. Dal Corso, S. de Gironcoli, S. Fabris, G. Fratesi, R. Gebauer, U. Gerstmann, C. Gougoussis, A. Kokalj, M. Lazzeri, L. Martin-Samos, N. Marzari, F. Mauri, R. Mazzarello, S. Paolini, A. Pasquarello, L. Paulatto, C. Sbraccia, S. Scandolo, G. Sclauzero, A. P. Seitsonen, A. Smogunov, P. Umari, and R. M. Wentzcovitch, *J. Phys.: Condens. Matter* **21**, 395502 (2009).
- ⁴²C. G. Broyden, *IMA J. Appl. Math.* **6**, 222 (1970).
- ⁴³D. Goldfarb, *Math. Comput.* **24**, 23 (1970).
- ⁴⁴D. F. Shanno, *Math. Comput.* **24**, 647 (1970).
- ⁴⁵K. K. Irikura, *J. Phys. Chem. Ref. Data* **36**, 389 (2007).
- ⁴⁶S. Plimpton, *J. Comput. Phys.* **117**, 1 (1995).
- ⁴⁷W. C. Swope, H. C. Andersen, P. H. Berens, and K. R. Wilson, *J. Chem. Phys.* **76**, 637 (1982).
- ⁴⁸D. Music and B. Stelzer, *Physics* **1**, 290 (2019).
- ⁴⁹H. J. C. Berendsen, J. P. M. van Postma, W. F. van Gunsteren, A. DiNola, and J. R. Haak, *J. Chem. Phys.* **81**, 3684 (1984).
- ⁵⁰J. Timmermann and Y. Lee, “IrO₂/RuO₂ training set and complexions,” <https://doi.org/10.6084/m9.figshare.16610488>, 2021.
- ⁵¹Since the GAP bulk lattice constant is not necessarily identical to the DFT one, the more common approach to constrain a certain fraction of innermost layers to bulk-like positions upon surface relaxation could impose artificial strain or require a delicate renormalization of atomic positions whenever a new training structure identified by the protocol is subjected to DFT computation.
- ⁵²J. Luo, *Energy Storage Mater.* **21**, 50 (2019).